Research Article

Analysis on the Dynamic Behavior of Space Shafting under Combined Load

Yan Zhao ⬦,[1] Fei Gao ⬦,[1,2] Yulei Xia ⬦,[1] Jinfang Gu,[3] Yameng Wang,[1] and Sen Zhao[1]

[1]*Luoyang Bearing Research Institute Co., Ltd., Luoyang 471039, China*
[2]*Department of Mechanical Engineering, Tsinghua University, Beijing 100083, China*
[3]*Shanghai Tianan Bearing Co., Ltd., Shanghai 200030, China*

Correspondence should be addressed to Fei Gao; 13698807332@126.com and Yulei Xia; zysxyl@outlook.com

The space shafting is the core component of the momentum exchange attitude control actuator for spacecraft. The dynamic behavior of space shafting has an important impact on the performance of the actuators. Based on the dynamic theory of rolling bearing, this paper presents a dynamic analysis model of space shafting for the interaction between bearing balls and oil-containing nonmetallic cage under combined loads. Also, the accuracy of the analysis model was verified through a high-speed camera system to conduct a cage speed test. In addition, the dynamic behavior of balls and cage under combined loads and the interaction between them is also analysed. The results show that the axial displacements of balls fluctuate periodically under combined loads, and the rotation speeds of balls and cage are easily affected by the load, presenting as the oscillation of speed. Also, the force between balls and cage increases as the load increases. The dynamic behavior of balls and cage could be effectively improved by avoiding excessive torque loads and limiting the axial preload to 40 N. The wear failure caused by unstable operation of bearings cannot be ignored. This model is more practical in completing simulation analysis of different operating conditions and structural parameters of the shafting system. It provides a theoretical reference for the structural design and performance analysis of space shafting.

1. Introduction

Space shafting operates in a high vacuum and microgravity space environment. It is the rotary support core of the spacecraft attitude control actuator. This institution realizes angular momentum exchange with the spacecraft by outputting angular momentum, so as to adjust the attitude of the spacecraft [1, 2]. The operational performance of the space shafting directly affects the reliability of the attitude control actuator and would cause disastrous consequences for the entire satellite once it fails.

Space shafting generally uses paired pretensioned angular contact ball bearings, with porous oil-containing nonmetallic cages as the rotation and lubrication core [3], whose lubrication performance is one of the most important factors limiting the service life of the shafting [4]. Space shafting operates at a high rotation speed for a long time and bears the combined action of axial force, radial force, and torque load. The combined load causes significant changes in bearing characteristics and motion state of the balls and easily leads to frequent friction between balls and cage, which would cause the polymer to damage the bearing lubrication system, causing precision failures of the space shafting due to wear [5, 6]. The report indicates that more than 50% of satellite attitude and orbit control system failures are caused by bearing shafting used in the flywheel [7]. Therefore, it is of great theoretical and practical significance to analyse the operation characteristics of the balls and cage in space shafting under combined loads and to study the interaction behavior between them.

The change in rotational speed has a significant impact on the vibration characteristics of the reaction flywheel. The imbalance of the flywheel system and the manufacturing parameters of the bearings affect the vibration amplitude of the entire machine [8, 9]. Halminen et al. [10] adopted a multibody dynamic contact model to establish a dynamic

analysis model for the magnetic suspension system supporting ball bearings and used numerical methods to study the dynamic performance of ball bearings with or without cages. Wang et al. [11, 12] considered the centrifugal force and gyroscopic moment of balls in high-speed angular contact ball bearings, developed a quasi-dynamic model of bearings without orbit control assumptions, and analysed the changes in contact angle, load distribution of bearings, and rotation/roll ratio of balls under high-speed conditions. The results also show that the role of centrifugal force is of great significance, especially in the design and analysis of rolling bearings under high-speed conditions.

A sliding dynamic model for angular contact ball bearings is established by Wang et al. [13]. The results show that the main reason for sliding is that the ball's revolution speed cannot reach the theoretical value and appropriate axial load can avoid the sliding behavior of the bearings. A model is established by Bai et al. [14] to analyse the vibration performance response of deep groove ball bearings in a wide temperature range. The analysis results show that the vibration speed of the inner ring increases with the increase of temperature under radial load. Zhang et al. [15] analysed the influence of lubricant types on the stability of high-speed angular contact ball bearing cages under different rotation speeds and load conditions and obtained a better matching combination. The structural parameters of the cage have a significant impact on the friction torque of the space bearing [16], and the shape of the pocket affects the operational stability, friction, and wear characteristics of the cage [17].

Wen et al. [18] conducted experimental research on the dynamic motion of the cage of ball bearings. The experimental results indicate that under the same working conditions, the cage motion is typically periodic in all three directions and the changes in axial and radial amplitudes are inconsistent. Li et al. [19] found that when the inner and outer rings rotate in the opposite direction, the speed of the cage greatly decreases, and the trajectory of the cage's center of mass oscillates irregularly on one side of the bearing center. As the rotation speed of the inner and outer rings increases, the axial displacement fluctuation of the cage increases. As the radial load increases, the axial fluctuation of the cage gradually decreases.

Chen et al. [20] found that during the process of entering and exiting the bearing area of the rolling element under high-speed conditions, one or more impacts occur between the rolling element and the cage. Choe et al. [21] studied the dynamic behavior of cage under high-speed conditions with mass imbalance. The impact of mass imbalance on the cage is evident with the increase in rotation speed. The unbalanced mass exacerbates the intermittent collision of the cage, causing rapid wear of the cage. Gao et al. [22] and Abele et al. [23] used high-speed cameras to photograph the cage during operation and obtained the centroid trajectory and rotation speed of the nonmetallic cage based on image processing methods to evaluate the stability of the cage during operation. Zhang et al. [24] and Ruan et al. [25] studied the oil discharge characteristics and lubricating oil migration characteristics of porous oil-containing cages and obtained

the friction coefficient and wear morphology between the cage and the steel ball at different temperatures.

Existing research mainly focuses on the dynamic behavior of the metal cage, while the research on porous oil-containing nonmetallic cages mostly focuses on the lubrication of the cage during oil discharge. However, the research on the dynamic behavior of balls and oil-containing nonmetallic cages under combined loads is still lacking. In view of this, a space shafting simulation model supported by angular contact ball bearings is established to analyse the dynamic behavior of the balls and cage under different rotation speeds and loads. The influence of rotation speed and load on the motion state of the balls and cage, as well as the degree of influence of the force between them, is also proposed. This could provide a basis for performance analysis and structural optimization of space shafting.

2. Dynamic Model of Space Shafting

In space shafting, there are many free degrees for balls and cages, and their motion behavior and stress state are also the most complex. In this section, the motion-free degrees of each element of space shafting bearing are considered. The dynamic differential equations of each component are listed based on the dynamic theory of rolling bearings. Finally, the dynamic analysis model of the spatial axis system is established.

2.1. Coordinate System and Motion Analysis. The space shafting is jointly supported by a pair of angular contact ball bearings, as shown in Figure 1. The rotation speed of the inner ring in the shafting is n, the outer ring is stationary, the axial preload is F_P, the radial load is F_r, and the torque load is M. The fixed coordinate system $\{o; x, y, z\}$, outer ring's coordinate system $\{o_i; x_i, y_i, z_i\}$, balls' coordinate system $\{o_b; x_b, y_b, z_b\}$, cage's coordinate system $\{o_c; x_c, y_c, z_c\}$, and pockets' coordinate system $\{o_p; x_p, y_p, z_p\}$ are established to describe the motion and relative position relationships of each element.

When the shafting rotates around the axis x_i at angular velocity ω_i, the balls rotate around the axis x_i at angular velocity ω_{iv} on the one hand and rotate around their own axes at angular velocity ω_{ib} on the other hand, as shown in Figure 2(a).

In figure 2(a), O_1 is the intersection of the ball rotation axis and the common rotation axis. β is the space attitude angle of the self-rotation axis. α_{li} and α_{le} are the contact angles between balls and inner and outer rings. M_{lg} is the gyro moment applied to balls. Subscripts i and e indicate inner and outer raceways and subscript l represents the left side bearing. The dynamic characteristics of the right-side bearing are similar to those of the left side, and the subscript r represents the right bearing. And the two bearings have similar dynamic characteristics. BX represents the axial displacement change of balls after being loaded. When the bearing only bears axial preload, each ball is uniformly loaded, and the movement path of balls in the inner and
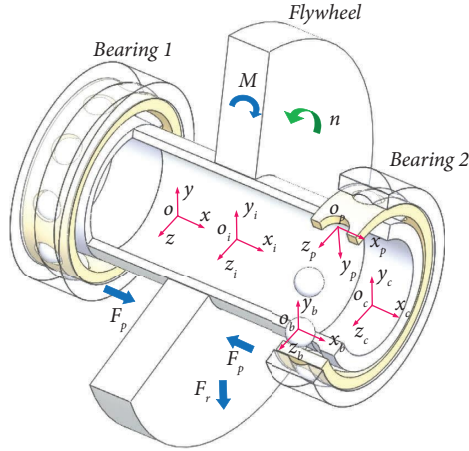
FIGURE 1: Schematic diagram of space shafting.

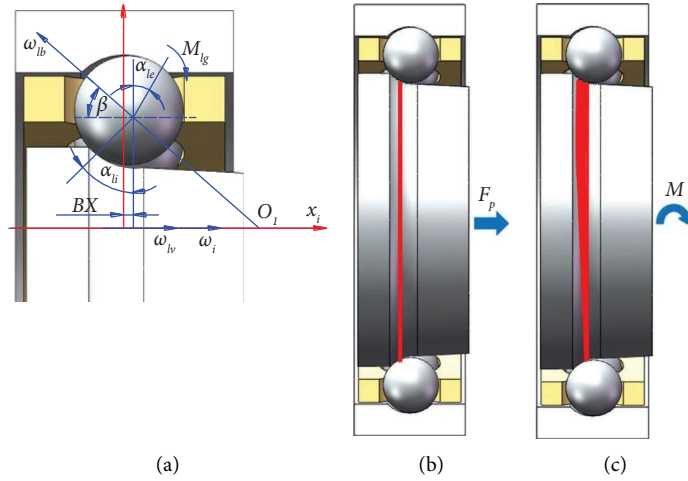(a)   (b)   (c)

FIGURE 2: Schematic diagram of ball's movement and its movement trajectory. (a) Schematic diagram of steel ball movement. (b) The motion path of a steel ball on a channel under axial force. (c) The motion path of a steel ball on a channel under moment load.

outer raceways are shown in Figure 2(b), where BX is a constant value. When axial-radial load or bending moment load is combined to the axial preload, the contact shape between balls and rings changes as shown in Figure 2(c), which shows that BX changes periodically.

2.2. Force and Motion Analysis of Cage.

Taking the $y - o - z$ plane as an example, the force and motion relationship between balls and cage is shown in Figure 3. The cage rotates at an angle of ω_{icm} and the balls rotate around the axis x at an angular velocity of ω_{lvj}, along with rotating around their own axes at an angular velocity of ω_{lrj}.

In Figure 3, Q_{lczj} and T_{lcvj} are the components of the normal and tangential forces between the balls and pockets in the $y_p - o_p - z_p$-plane, respectively. F_{lcy} and F_{lcz} are the normal and tangential forces of the guidance clearance on cage, respectively. ψ_{lc} is the angle between the coordinate system $\{o_c; y_c, z_c\}$ and $\{o_e; y_e, z_e\}$. φ_{lj} is the azimuth angle of the j th ball.

The normal force Q_{lczj} and tangential force T_{lcvj} between balls and cage can be expressed as follows:
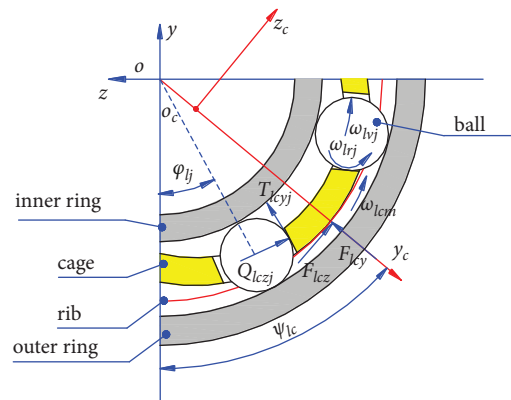
FIGURE 3: Schematic diagram of bearing movement and interaction force.

$$Q_{\mathrm{lczj}} = K_{\mathrm{bc}}\delta_{\mathrm{lczj}}^{1.5} + C_{\mathrm{bc}}v_{\mathrm{lczj}}, \tag{1}$$

$$T_{\mathrm{lcvj}} = f_{\mathrm{sot}}Q_{\mathrm{lczj}}, \tag{2}$$

where K_{bc} is the contact stiffness; δ_{lczj} is the contact deformation; C_{bc} is the damping coefficient; and v_{lczj} is the speed of balls relative to pockets. T_{lcvj} depends on the friction coefficient and the normal force at the contact, where $f_{sot} = 0.085$.

In summary, the dynamic differential equation of cage can be expressed as follows:

$$
\begin{cases}
m_k \ddot{x}_{lc} = \sum_{j=1}^{z} \left(Q_{lcxj} + T_{lcxj} + T_{lcx} \right), \\[2mm]
m_{lc} \ddot{y}_{lc} = F_{lcz} \sin \psi_{lc} + F_{lcy} \sin \psi_k + \sum_{j=1}^{z} \left[Q_{lczj} \sin \varphi_{lj} + T_{lcyj} \cos \varphi_{lj} \right] - G_{lc}, \\[2mm]
m_{lc} \ddot{z}_{lc} = F_{lcy} \sin \psi_{lc} - F_{lcz} \sin \psi_k + \sum_{j=1}^{z} \left[Q_{lcyj} \sin \varphi_{lj} - T_{lczj} \cos \varphi_{lj} \right], \\[2mm]
J_{lcx} \dot{\omega}_{lcx} = \sum_{j=1}^{z} \left[Q_{lczj} \frac{d_m}{2} + T_{lcyj} \frac{D_w}{2} \right] + M_{lcx}, \\[2mm]
J_{lcy} \dot{\omega}_{lcy} = \sum_{j=1}^{z} \left[\left(Q_{lcxj} + T_{lcxj} \right) \frac{d_m}{2} \sin \varphi_{lj} \right], \\[2mm]
J_{lcz} \dot{\omega}_{lcz} = \sum_{j=1}^{z} \left[\left(Q_{lcxj} + T_{lcxj} \right) \frac{d_m}{2} \cos \varphi_{lj} \right],
\end{cases}
\tag{3}
$$

where m_{lc} is the mass of cage; $\ddot{x}_{lc}$, $\ddot{y}_{lc}$, and $\ddot{z}_{lc}$ are the accelerations of the center of mass of cage; J_{lcx}, J_{lcy}, and J_{lcz} represent the rotational inertia of cage, ω_{lcx}, ω_{lcy}, and ω_{lcz} are the angular velocities of cage. D_w is the diameter of balls, d_m is the diameter of the bearing pitch circle, Z is the number of balls, and G_{lc} is the gravity of cage. M_{lcx} represents the torque of the guide rib to cage, and the subscript j represents the j th ball.

2.3. Force and Motion Analysis of Balls.
Taking balls of the left end bearing in the space shafting system as an example, their stress under radial and axial loads is shown in Figures 4(a)–4(c). Q_{lij} and Q_{lej} are normal contact load between the balls and the inner ring and outer ring, and $T_{l\eta ej}$, $T_{l\eta ij}$, $T_{l\xi ej}$, and $T_{l\xi ij}$ are the drag forces between balls and the rings. Q_{lcxj} is the normal contact load between balls and cage in axial direction, $P_{lR\eta j}$ and $P_{lR\xi j}$ are the rolling friction resistance of balls, and $P_{lS\eta j}$ and $P_{lS\eta j}$ are their sliding friction resistance. $F_{h\eta ij}$, $F_{h\eta ej}$, $F_{h\xi ij}$, and $F_{h\xi ej}$ are the horizontal components of the fluid dynamic pressures acting on the centre of balls, and $F_{l\eta ij}$, $F_{l\eta ej}$, $F_{l\xi ij}$, and $F_{l\xi ej}$ are the hydrodynamic friction forces at the entrance where the balls contact the inner and outer rings. Subscripts η and ξ refer to the major and minor axis directions of the contact ellipse between balls and rings, respectively.

The dynamic differential equations of balls can be expressed as follows:
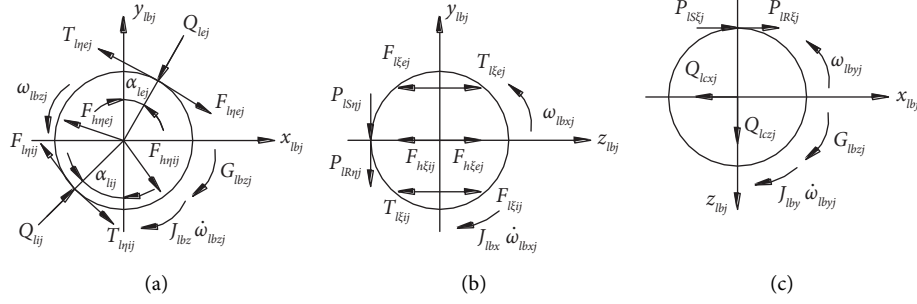
FIGURE 4: Force acting on balls. (a) Force on the $x_{bj} - o_{bj} - y_{bj}$ plane. (b) Force on the $y_{bj} - o_{bj} - z_{bj}$ plane. (c) Force on the $x_{bj} - o_{bj} - z_{bj}$ plane.

$$
\begin{cases}
\begin{aligned}
m_{lb}\ddot{x}_{lbj} &= Q_{lij}\sin\alpha_{lij} - Q_{lej}\sin\alpha_{lej} + T_{l\eta ij}\cos\alpha_{lij} - T_{l\eta ej}\cos\alpha_{lej} + F_{l\eta ij}\cos\alpha_{lij} \\
&\quad + F_{l\eta ej}\cos\alpha_{lej} + F_{h\eta ij}\cos\alpha_{lij} - F_{h\eta ej}\cos\alpha_{lej} + P_{lS\xi j} + P_{lR\xi j} - Q_{lcxj}, \\[4pt]
m_{lb}\ddot{y}_{lbj} &= Q_{lij}\cos\alpha_{lij} - Q_{lej}\cos\alpha_{lej} - T_{l\eta ij}\sin\alpha_{lij} + T_{l\eta ej}\sin\alpha_{lej} + F_{l\eta ij}\sin\alpha_{lij} \\
&\quad - F_{l\eta ej}\sin\alpha_{lej} - F_{h\eta ij}\sin\alpha_{lij} + F_{h\eta ej}\sin\alpha_{lej} - P_{lS\eta j} - P_{lR\eta j}, \\[4pt]
m_{lb}\ddot{z}_{lbj} &= T_{l\xi ej} - T_{l\xi ij} + F_{l\xi ij} - F_{l\xi ej} + F_{h\xi ij} - F_{h\xi ej} + Q_{lczj}, \\[4pt]
J_{lbx}\dot{\omega}_{lbxj} &= \left(T_{l\xi ej} - F_{l\xi ej}\right)\frac{D_w}{2}\cos\alpha_{lej} + \left(T_{l\xi ij} - F_{l\xi ij}\right)\frac{D_w}{2}\cos\alpha_{lij} - \left(P_{lS\eta j} + P_{lR\eta j}\right)\frac{D_w}{2}, \\[4pt]
J_{lby}\dot{\omega}_{lbyj} &= \left(F_{l\xi ej} - T_{l\xi ej}\right)\frac{D_w}{2}\sin\alpha_{lej} + \left(F_{l\xi ij} - T_{l\xi ij}\right)\frac{D_w}{2}\sin\alpha_{lij} - \left(P_{lS\xi j} + P_{lR\xi j}\right)\frac{D_w}{2} - G_{lyj}, \\[4pt]
J_{lbz}\dot{\omega}_{lbzj} &= \left(T_{l\eta ej} - F_{l\eta ij} + T_{l\eta ij} - F_{l\eta ej}\right)\frac{D_w}{2} - G_{lzj},
\end{aligned}
\end{cases}
\tag{4}
$$

where m_{lb} is the mass of each ball, $\ddot{x}_{lbj}$, $\ddot{y}_{lbj}$, and $\ddot{z}_{lbj}$ represent the acceleration of the centre of mass of balls, and ω_{lbxj}, ω_{lbyj}, and ω_{lbzj} are the angular velocities of balls.

2.4. Force and Motion Analysis of the Shafting. The load applied to the inner ring as well as shafting during operation is shown in Figure 5, where θ is the inclination angle of the
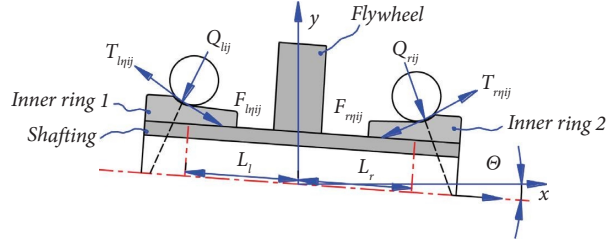
FIGURE 5: Force acting on shaft and inner rings.

shafting after being loaded; L_l and L_r are the distances between the radial load and the two bearings. The dynamic differential equations of the space shafting are as follows:

$$
\begin{cases}
m_s \ddot{x}_s = \sum_{j=1}^{z}\left(Q_{\mathrm{rij}}\sin\alpha_{\mathrm{rij}} - Q_{\mathrm{lij}}\sin\alpha_{\mathrm{lij}} + \left(T_{r\eta ij} - F_{r\eta ij}\right)\cos\alpha_{\mathrm{rij}} - \left(T_{l\eta ij} - F_{l\eta ij}\right)\cos\alpha_{\mathrm{lij}}\right), \\[2mm]
m_s \ddot{y}_s = \sum_{j=1}^{z}\left[\begin{array}{c}\left(-Q_{\mathrm{rij}}\cos\alpha_{\mathrm{rij}} + \left(T_{r\eta ij} - F_{r\eta ij}\right)\sin\alpha_{\mathrm{rij}}\right)\cos\varphi_{\mathrm{rj}} \\ +\left(-Q_{\mathrm{lij}}\cos\alpha_{\mathrm{lij}} + \left(T_{l\eta ij} - F_{l\eta ij}\right)\sin\alpha_{\mathrm{lij}}\right)\cos\varphi_{\mathrm{lj}}\end{array}\right] + F_r, \\[4mm]
m_s \ddot{z}_s = \sum_{j=1}^{z}\left[\begin{array}{c}\left(-Q_{\mathrm{rij}}\cos\alpha_{\mathrm{rij}} + \left(T_{r\xi ij} - F_{r\xi ij}\right)\right)\sin\varphi_{\mathrm{rj}} \\ +\left(-Q_{\mathrm{lij}}\cos\alpha_{\mathrm{lij}} + \left(T_{l\xi ij} - F_{l\xi ij}\right)\right)\sin\varphi_{\mathrm{rj}}\end{array}\right], \\[4mm]
J_{\mathrm{sy}}\dot{\omega}_{\mathrm{sy}} = M_y + \sum_{j=1}^{z}\left[\begin{array}{c}\left(0.5d_m - (f_i - 0.5D_w)\cos\alpha_{\mathrm{lj}}\right)\left(Q_{\mathrm{lij}}\sin\alpha_{\mathrm{lij}} + \left(T_{r\eta ij} - F_{r\eta ij}\right)\cos\alpha_{\mathrm{lij}}\right)\sin\varphi_{\mathrm{lj}} \\ -\left(0.5d_m - (f_i - 0.5D_w)\cos\alpha_{\mathrm{rj}}\right)\left(Q_{\mathrm{rij}}\sin\alpha_{\mathrm{rij}} + \left(T_{r\eta ij} - F_{r\eta ij}\right)\cos\alpha_{\mathrm{rij}}\right)\sin\varphi_{\mathrm{rj}} \\ +L_l\left(-Q_{\mathrm{rij}}\cos\alpha_{\mathrm{rij}} + \left(T_{r\xi ij} - F_{r\xi ij}\right)\sin\varphi_{\mathrm{rj}}\right) \\ -L_r\left(-Q_{\mathrm{lij}}\cos\alpha_{\mathrm{lij}} + \left(T_{l\xi ij} - F_{l\xi ij}\right)\sin\varphi_{\mathrm{lj}}\right)\end{array}\right], \\[8mm]
J_{\mathrm{sz}}\dot{\omega}_{\mathrm{sz}} = M_z + \sum_{j=1}^{z}\left[\begin{array}{c}\left(0.5d_m - (f_i - 0.5D_w)\cos\alpha_{\mathrm{lj}}\right)\left(Q_{\mathrm{lij}}\sin\alpha_{\mathrm{lij}} + \left(T_{r\eta ij} - F_{r\eta ij}\right)\cos\alpha_{\mathrm{lij}}\right)\cos\varphi_{\mathrm{lj}} \\ -\left(0.5d_m - (f_i - 0.5D_w)\cos\alpha_{\mathrm{rj}}\right)\left(Q_{\mathrm{rij}}\sin\alpha_{\mathrm{rij}} + \left(T_{r\eta ij} - F_{r\eta ij}\right)\cos\alpha_{\mathrm{rij}}\right)\cos\varphi_{\mathrm{rj}} \\ +L_l\left(-Q_{\mathrm{rij}}\cos\alpha_{\mathrm{rij}} + \left(T_{r\xi ij} - F_{r\xi ij}\right)\sin\varphi_{\mathrm{rj}}\right)\cos\varphi_{\mathrm{rj}} \\ -L_r\left(-Q_{\mathrm{lij}}\cos\alpha_{\mathrm{lij}} + \left(T_{l\xi ij} - F_{l\xi ij}\right)\sin\varphi_{\mathrm{lj}}\right)\cos\varphi_{\mathrm{lj}}\end{array}\right],
\end{cases}
\tag{5}
$$

where m_s is the overall mass of the shaft and inner ring, $\ddot{x}_s$, $\ddot{y}_s$, and $\ddot{z}_s$ are the accelerations of the center of mass of the shaft and the inner ring as a whole, J_{sy} and J_{sz} are the rotational inertia of the shaft and inner ring as a whole, and f_i is the coefficient of curvature radius of the inner ring groove.

3. Calculation and Analysis

The research object is a space shafting supported by a pair of bearings. The type of bearing is angular contact ball bearing and their parameters are shown in Table 1. First, the cage speed test was conducted to analyse the accuracy of the mathematical model. The dynamic behavior of balls under different loads and speeds as well as the interaction between them is analysed to explore the impact of

operating conditions on the dynamic characteristics of space shafting.

3.1. Experiments. Figure 6(a) shows the speed measurement platform for the cage of space shafting to verify the reliability of the spatial axis system dynamics model; the parameters of the high-speed camera are shown in Table 2. The high-speed photography technology, as an efficient and accurate non-contact testing method, can avoid modification and damage to bearing and related structures, without the need for customized cages for testing. The space shafting is driven by a driven system, which synchronously records the speed of the DC motor. The high-speed camera captures the cage during operation, and the camera's acquisition frequency is sufficient to restore the continuous motion of the cage. Three

TABLE 1: Parameters of bearings in space shafting.

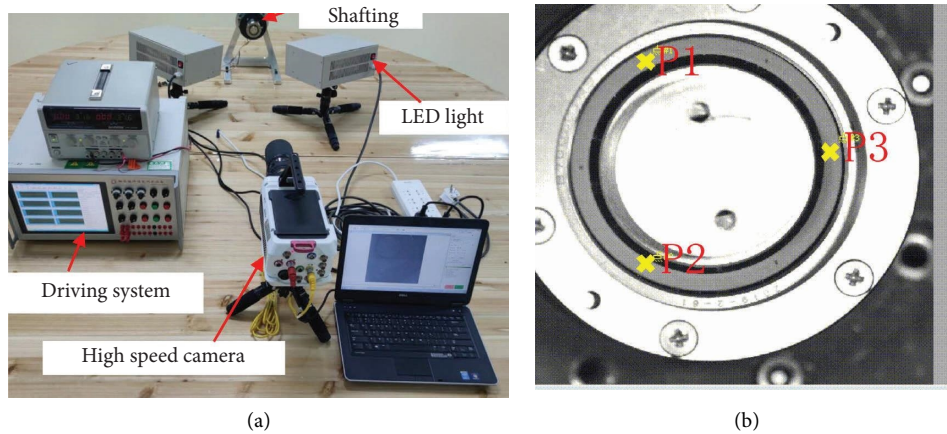| Structure parameter	Value
Pitch diameter (mm)	18
Diameter of balls (mm)	4
Number of balls	10
Contact angle (°)	15
Internal groove curvature coefficient (f_i)	0.53
External groove curvature coefficient f_e	0.55

(a)

(b)

FIGURE 6: The speed measurement platform and the marking points. (a) Bearing cage speed test system. (b) Cage marker.

TABLE 2: Parameters of the high-speed camera.

Parameter	Value
Full frame shooting speed (f/s)	7530
Full shooting speed (f/s)	1.4 million
Maximum resolution	1280×800
Pixel size (mm)	0.02
Minimum exposure time (s)	0.001
Error (%)	< 0.11

marking points, $P1$, $P2$, and $P3$, are set in the circumferential direction of the cage end face, as shown in Figure 6(b). By processing the pixel position information of the marking points in the images captured by the high-speed camera, the rotation speed of the cage could be obtained.

Due to the limited shooting frequency of the high-speed camera, experiments can only be conducted at medium-to-low speed stages. When $F_p = 40$N, $F_r = 20$N, and $n = 8000$ r/min, the experimental and simulation values of cage speed are shown in Figure 7. The simulation value is slightly higher than the experimental value, and the measured cage speed changes significantly, while the fluctuation of the simulation results is relatively small. The position error of the marked points on the cage and the speed error of the DC motor may affect the measurement results of the cage speed during the test process. This results in a certain error between the experimental and simulated values. It is believed that the simulation results and experimental results have high consistency within the error range, which verifies the accuracy of the spatial axis analysis model.
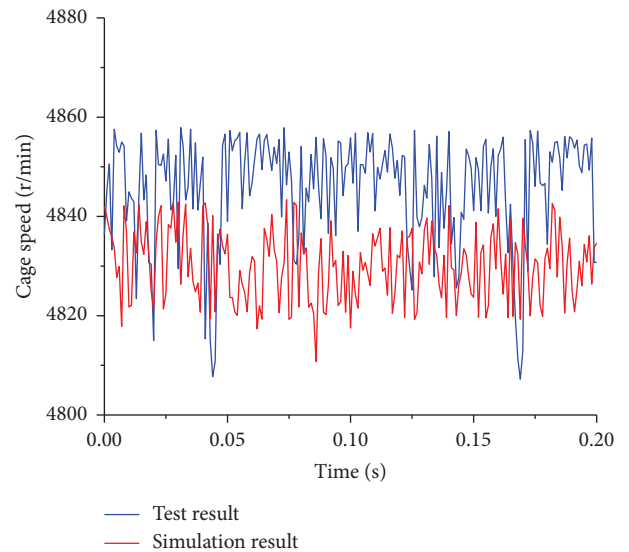

FIGURE 7: Experimental and simulation values of cage speed.

3.2. Influence of Speed on the Dynamic Performance of Shafting Bearings. The force between bearing balls and cage at different rotation speeds in the case of $F_r = 60$ N and $F_P = 20$ N is shown in Figure 8. As the rotation speed increases, the force between balls and cage gradually increases. The trend of the force between balls and cage is gentle when the rotational speed is less than 40000 r/min. However, when the speed increases from 40000 r/min to 50000 r/min, the force increases sharply. This is because when the speed is greater than 40000 r/min, the centrifugal force on the ball is too
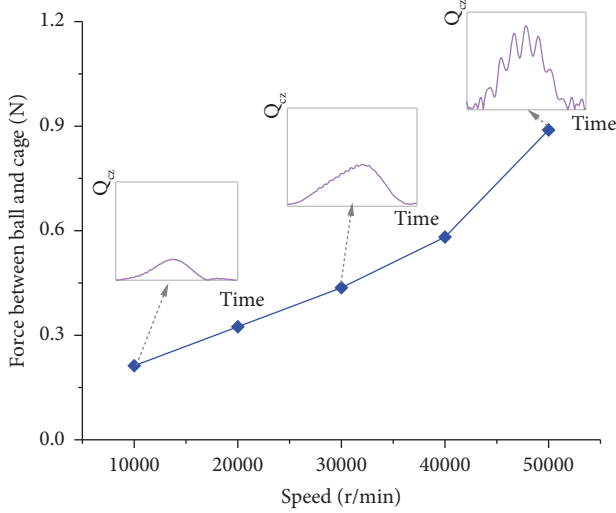
Figure 8: Influence curve of speed on the force between balls and cage.

Figure 9: Displacement of balls in the x-axis direction at different rotational speeds.

large, which weakens the dragging effect of the ring on the ball. According to the time-domain diagram of the force, the contact force curve between balls and cage is smooth at speeds of 10000 r/ min and 30000 r/ min. When the rotation speed is 50000 r/ min, there is a significant fluctuation in the force between balls and the cage, and there are multiple peaks within one action cycle.

The displacement of balls in the x-axis direction at different rotational speeds is shown in Figure 9. Under radial-axial load, the centres of mass of balls exhibit sinusoidal periodic change in x-axis direction. Under low-speed conditions, the displacement of balls in the x-axis direction during revolution is relatively large. When the speed is 50000 r/ min, the maximum value is about 0.0065 mm. However, at this time, the fluctuation of the displacement is relatively small, with a fluctuation range of about 0.005 mm. As the rotation speed increases, the maximum displacement of balls in the x-axis direction gradually decreases and the fluctuation range increases to 0.01 mm when the rotational speed is 50000 r/ min.

Figure 10 shows the revolution speeds of balls and cage at different rotation speeds of the shafting. When the rotation speed is 10000 r/ min, the revolution speeds of balls and cage change in a sinusoidal manner, with no abnormal jump and significant change, as shown in Figure 10(a), which means that the interaction between balls and cage is stable, so the contact force is small and stable. As the rotation speed increases, the axial movement of balls gradually increases and the revolution speed begins to exhibit irregular abnormal fluctuations, as shown in Figure 10(b). When the speed increases to 50000 r/ min, there is a wavy change in the revolution speeds of balls and cage. The maximum speed change is about 70 r/ min, as shown in Figure 10(c).

The reasons for the above phenomenon are as follows. As the rotation speed increases, the centrifugal force of balls gradually increases and the contact angle between balls and outer ring decreases, that is, the displacement of the balls in the x-axis direction decreases. But as the axial speed
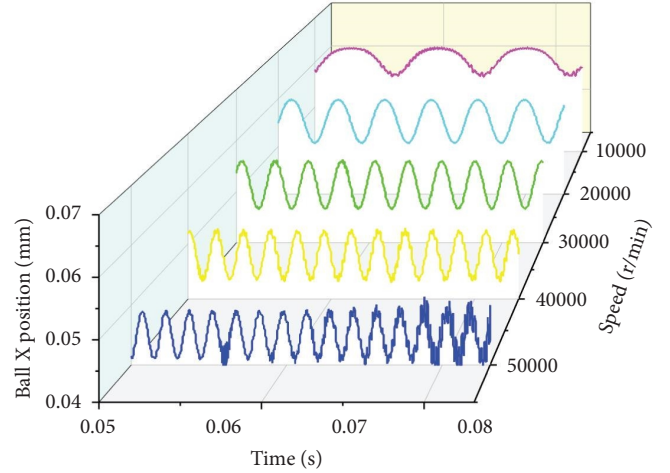
increases, the contact state between balls and the ring is no longer stable under the influence of centrifugal force, and the position change of balls in x-axis direction significantly increases. The change in the contact position between balls and the ring causes fluctuations in the revolution speed of balls, which affects the rotation of cage and induces an unstable contact between balls and pockets. Therefore, the contact force between balls and cage fluctuates. The fluctuation of contact force will change the movement state of the cage. In severe cases, it can cause the cage to lose stability during movement. This will cause the cage to fail due to wear.

3.3. Influence of Preload on the Dynamic Performance of Shafting Bearings. This section analyses the rotation speed and force between balls and cage within the range of $F_P = 20 \sim 70$ N when Fr = 60 N and $n = 50000$ r/ min. Figure 11 shows the variation trend of the force between balls and cage under different rotation speeds and preloads. As can be seen from Figure 11, the force gradually decreases and increases as the axial preload increases, and both larger and smaller preloads cause frequent fluctuations in the force. When $F_P = 40$ N, the force between the balls and cage is the smallest, and the force changes smoothly over time.

The displacement of balls in the x-axis direction under different preloads is shown in Figure 12. The displacement of the centre of mass of balls in the x-axis direction increases with the increase of preload, and the fluctuation value of the displacement decreases with the increase of preload. When $F_P = 20$ N, the movement of balls in the x-axis direction showed significant fluctuations, with a fluctuation range of 0.01 mm. When $F_P = 60$ N, the displacement fluctuation range of balls in the x-axis direction was 0.004 mm.

Figure 13 shows the variation trend of the revolution speeds of balls and cage with preload at $n = 50000$ r/ min. As can be seen from Figure 13(a), when the preload is small, there are many fluctuations in the revolution speed of balls and cage. When $F_P = 40$ N, the revolution speeds of balls changes smoothly and the fluctuation value of cage's speed
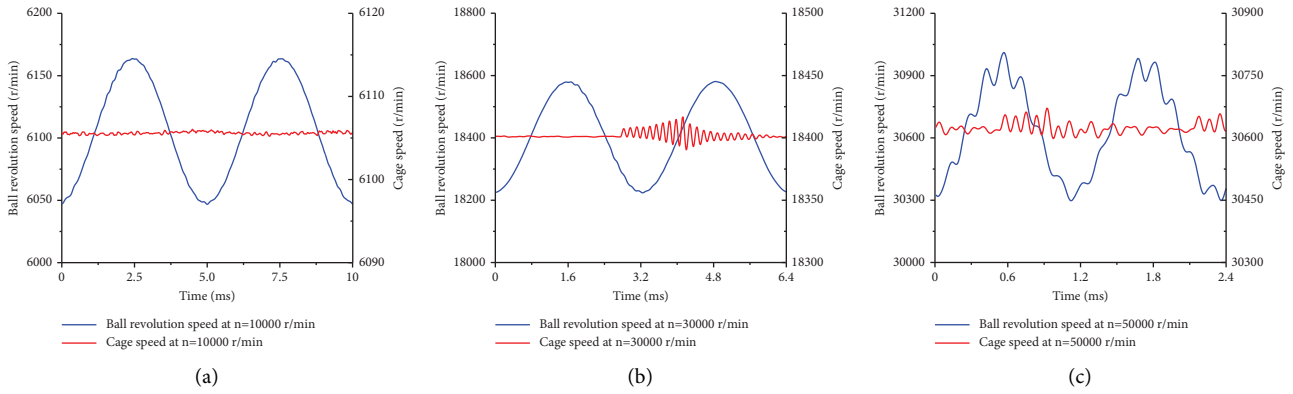
FIGURE 10: Revolution speed of balls and speed of cage at different rotational speeds. (a) At a speed of 10000 r/ min. (b) At a speed of 30000 r/ min. (c) At a speed of 50000 r/ min.
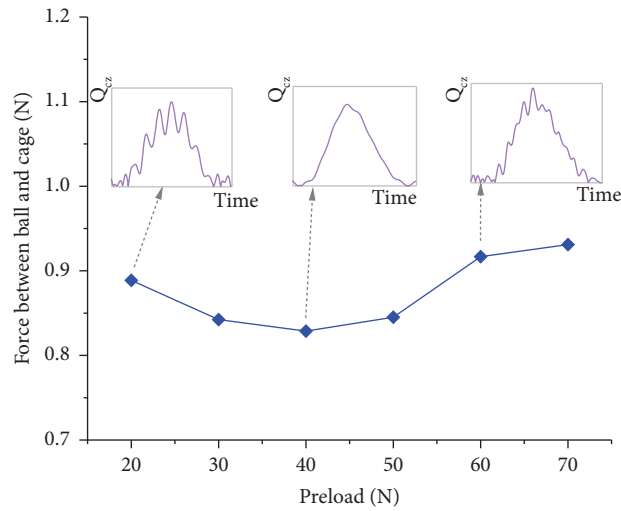

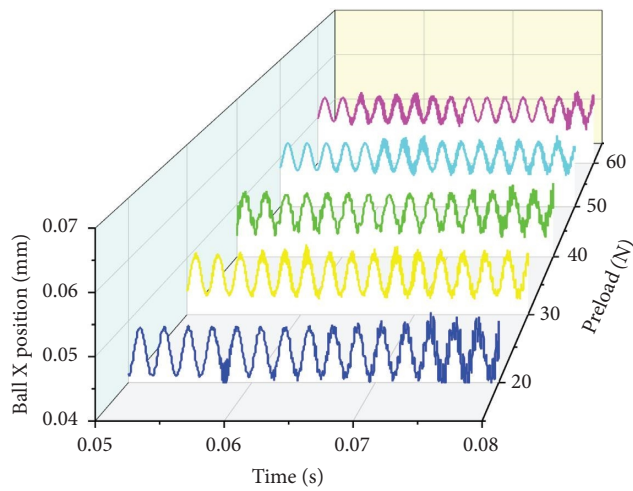FIGURE 11: Force between balls and cage under different rotating speeds and preloads.

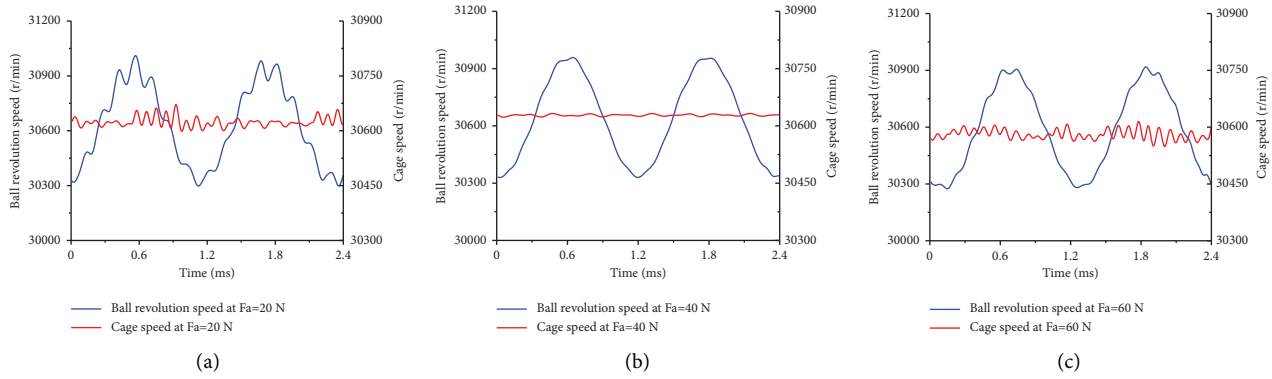FIGURE 12: The ball trajectory at F_p = 40 N and n = 10000 r/ min.

FIGURE 13: Speed of balls and cage at $F_r = 60\,\text{N}$ and $n = 50000\,\text{r/min}$. (a) $F_p = 20\,\text{N}$. (b) $F_p = 40\,\text{N}$. (c) $F_p = 60\,\text{N}$.

decreases. However, as the preload increases to 60 N, the stability of the revolution speed of balls decreases, and there is a significant fluctuation in cage speed, as shown in Figure 13(c).

The reasons for the influence of preload on the dynamic performance of shaft bearings are as follows. Under radial force and small preload conditions, the balls generate significant centrifugal force during the high-speed operation. The unstable operation of balls results in frequent changes in the contact angle with the rings, causing severe fluctuations in the revolution speed of balls. Therefore, the force between balls and cage is relatively large and the collision frequency is high. When the axial load is moderate, the contact load between balls and rings increases, which weakens the centrifugal effect that causes the balls to rotate at high speed. The revolution speed of balls and cage changes stably, the slower balls slide slightly under the action of cage, and the force between is relatively stable. As the preload continues to increase, the contact load between balls and the rings becomes more sufficient. The collision between balls and cage is difficult to change the movement state of balls, and the sliding effect of balls is weakened, thereby increasing the force between balls and pockets.

3.4. Influence of Torque Load and Preload on the Dynamic Performance of Bearings. When $F_P = 40\,\text{N}$ and $n = 10000\,\text{r/min}$, the force between balls and cage under different torque loads is shown in Figure 14. As the torque load increases, the overall interaction force between balls and cage shows a trend of first increasing, then decreasing, and then rapidly increasing. According to the time-domain diagram of the force, there is a large peak and a small peak in the force between balls and cage under torque load.

Figure 15 shows the displacement of the steel ball in the x-axis direction when $M = 1 \sim 5\,\text{N} \cdot \text{m}$. When the torque load is small, the overall operation of balls is stable, and the axial displacement of balls hardly changes with increasing time. As the torque load increases, the displacement change in the x-axis direction of balls gradually increases, and the displacement curve shows the "V" shape fluctuation over time.

Figure 15 shows the effect of torque load on the revolution speed of balls and the speed of cage. When $M = 0\,\text{N} \cdot \text{m}$, the bearing only supports axial force, and the
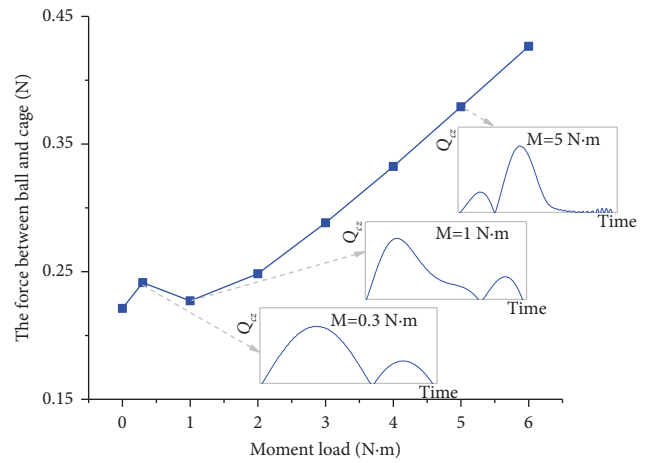

FIGURE 14: Effect of load on the force between ball and cage.

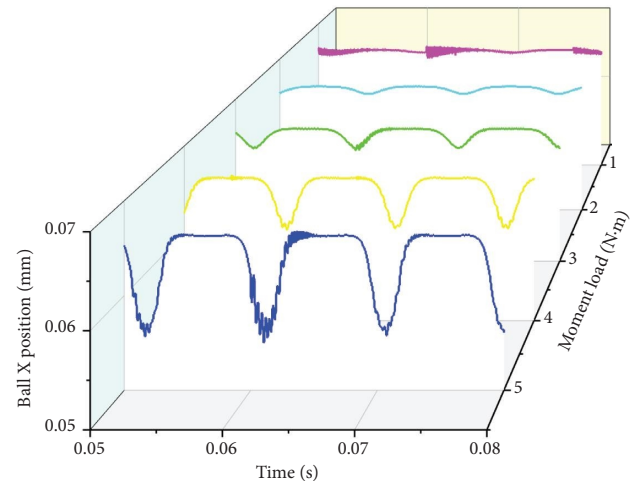FIGURE 15: The ball trajectory at $F_P = 50\,\text{N}$ and $M = 1 \sim 5\,\text{N} \cdot \text{m}$.

force on each ball is consistent with the movement of the turntable, so the force between the balls and cage is relatively small. When $M = 0.3\,\text{N} \cdot \text{m}$, the load on each rolling element is not uniform, causing a certain degree of fluctuation in the rotation speed of cage, as shown in Figure 16(a). At this point, the position relationship between balls and pockets is
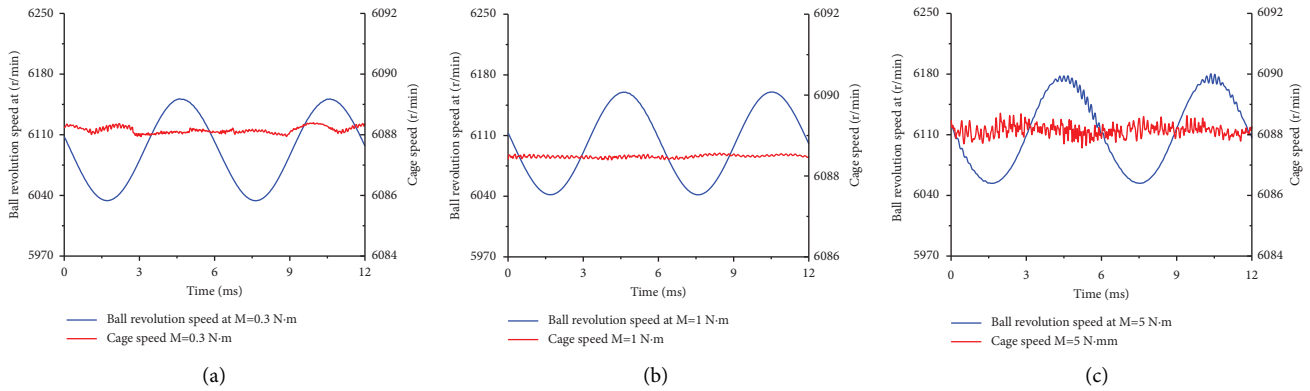
FIGURE 16: Effect of moment load on the speed of balls. (a) $M = 0.3\,\text{N} \cdot \text{m}$. (b) $M = 1\,\text{N} \cdot \text{m}$. (c) $M = 5\,\text{N} \cdot \text{m}$.

adjusted through a strong mutual contact, and the force between balls and cage is relatively large. When $M = 1\,\text{N} \cdot \text{m}$, some balls are heavily loaded while others are lightly loaded. The positional relationship between balls and pockets could be adjusted through the small sliding of balls, and the revolution speeds of balls and cage are relatively stable, as shown in Figure 16(b). As the torque load continues to increase, some balls undergo unloading, and the balls repeatedly enter and exit the bearing and unloading areas. The speed fluctuates after the balls leave the bearing area, causing frequent fluctuations in the speed of cage, as shown in Figure 16(c). Therefore, the force between balls and cage increases sharply.

4. Conclusions

Considering the contact characteristics of balls and porous oil-containing nonmetallic cages, this paper establishes a dynamic analysis model of a space shafting system supported by a pair of angular contact ball bearings. Based on this model, the dynamic behavior of bearing balls and cages under combined loads as well as the interaction forces was analysed. The main conclusions are as follows:

(1) Based on the high-speed camera system, the operating speed of cage could be tested. Simulation results and experimental results present high consistency under the same operating conditions, verifying the accuracy of the space shafting simulation analysis model.

(2) Radial force and torque load change the motion trajectory of the rolling element, causing fluctuations in the displacement of balls in the x-axis direction, and the torque load has a more significant impact on the dynamic behavior of balls and cage.

(3) As the rotation speed of the space shafting increases, the force between bearing balls and cage gradually increases, and the fluctuation of the revolution speeds of balls and cage gradually increases.

(4) The force between balls and cage decreases first and then increases with the increase of preload, and the oscillation range of the revolution speeds of balls and cage decreases first and then increases with the

increase of preload. When the preload is 40 N, it helps to improve the dynamic behavior of balls and cage.

(5) As the torque load increases, the force between balls and cage first increases, then decreases, and then rapidly increases. The revolution speeds of balls and cage fluctuate sharply under strong torque load conditions. The operational stability of balls and cage could be effectively improved through controlling the torque load borne by the space shafting to be less than the torque load when the bearing is unloaded.

Data Availability

The data used to support the findings of this paper are available from the corresponding author upon request.

Conflicts of Interest

The authors declare that there are no conflicts of interest regarding the publication of this paper.

Acknowledgments

References

[1] T. Wu, Y. Zhuang, B. Fan et al., "Multidomain feature fusion for varying speed bearing diagnosis using broad learning system," *Shock and Vibration*, vol. 2021, Article ID 6627305, 8 pages, 2021.

[2] A. Olivares and E. Staffetti, "Time-optimal attitude scheduling of a spacecraft equipped with reaction wheels," *International Journal of Aerospace Engineering*, vol. 2018, Article ID 5947521, 14 pages, 2018.

[3] K. Li, Y. Liu, J. Liu, and W. Chen, "Study on the performance of a designed annular piezoelectric microjet for active

lubrication of space bearing," *IEEE Transactions on Industrial Electronics*, vol. 69, no. 3, pp. 2728–2736, 2021.

[4] D. Zhang, C. Wang, Q. Wang, and T. Wang, "High thermal stability and wear resistance of porous thermosetting heterocyclic polyimide impregnated with silicone oil," *Tribology International*, vol. 140, Article ID 105728, 2019.

[5] Y. Zhang, S. Zhang, G. Zhou, J. Zhang, T. Qing, and N. Zhou, "The friction and wear behaviors of polyimide bearing retainer under point-contact condition," *Industrial Lubrication & Tribology*, vol. 72, no. 7, pp. 931–936, 2020.

[6] K. Sathyan, K. Gopinath, S. H. Lee, and H. Y. Hsu, "Bearing retainer designs and retainer instability failures in spacecraft moving mechanical systems," *Tribology Transactions*, vol. 55, no. 4, pp. 503–511, 2012.

[7] S. Zhang, J. Shi, and J. Wang, "Satellite on-board failure statistics and analysis," *Spacecraft Engineering*, vol. 19, no. 4, pp. 41–46, 2010.

[8] C. Hodge, A. Stabile, G. Aglietti, and G. Richardson, "The effect of assembly and static unbalance on reaction wheel assembly bearing harmonics," *Corporate Emergency Access System Space Journal*, vol. 13, no. 2, pp. 269–289, 2020.

[9] H. Alkomy and J. Shan, "Modeling and validation of reaction wheel micro-vibrations considering imbalances and bearing disturbances," *Journal of Sound and Vibration*, vol. 492, no. 1, Article ID 115766, 2021.

[10] O. Halminen, J. F. Aceituno, J. L. Escalona, J. Sopanen, and A. Mikkola, "Models for dynamic analysis of backup ball bearings of an AMB-system," *Mechanical Systems and Signal Processing*, vol. 95, pp. 324–344, 2017.

[11] W. Z. Wang, L. Hu, S. G. Zhang, and L. J. Kong, "Modeling high-speed angular contact ball bearing under the combined radial, axial and moment loads," *Proceedings of the Institution of Mechanical Engineers- Part C: Journal of Mechanical Engineering Science*, vol. 228, no. 5, pp. 852–864, 2014.

[12] W. Z. Wang, L. Hu, S. G. Zhang, Z. Zhao, and S. Ai, "Modeling angular contact ball bearing without raceway control hypothesis," *Mechanism and Machine Theory*, vol. 82, pp. 154–172, 2014.

[13] Y. Wang, W. Wang, S. Zhang, and Z. Zhao, "Investigation of skidding in angular contact ball bearings under high speed," *Tribology International*, vol. 92, pp. 404–417, 2015.

[14] X. Bai, H. Zheng, Z. Wang, and Z. Wang, "Raceway defect frequency deviation of full-ceramic ball bearing induced by fit clearance in wide temperature ranges," *Shock and Vibration*, vol. 2021, Article ID 6650798, 13 pages, 2021.

[15] W. Zhang, S. Deng, G. Chen, and Y. Cui, "Impact of lubricant traction coefficient on cage's dynamic characteristics in high-speed angular contact ball bearing," *Chinese Journal of Aeronautics*, vol. 30, no. 2, pp. 827–835, 2017.

[16] S. Jiang, X. Chen, J. Gu, and X. Shen, "Friction moment analysis of space gyroscope bearing with ribbon cage under ultra-low oscillatory motion," *Chinese Journal of Aeronautics*, vol. 27, no. 5, pp. 1301–1311, 2014.

[17] S. Chen, X. Chen, Q. Shuai, and J. Gu, "Effects of cage pocket shapes on dynamics of angular contact ball bearings," *Tribology Online*, vol. 15, no. 5, pp. 343–355, 2020.

[18] B. Wen, H. Ren, H. Zhang, and Q. Han, "Experimental investigation of cage motions in an angular contact ball bearing," *Proceedings of the Institution of Mechanical Engineers- Part J: Journal of Engineering Tribology*, vol. 231, no. 8, pp. 1041–1055, 2017.

[19] Q. Li, X. Chen, T. Zhang, S. Chen, and J. Gu, "Experimental research on cage dynamic characteristics of angular contact ball bearing," *Mechanics & Industry*, vol. 20, no. 2, p. 204, 2019.

[20] L. Chen, X. Xia, H. Zheng, and M. Qiu, "Chaotic dynamics of cage behavior in a high-speed cylindrical roller bearing," *Shock and Vibration*, vol. 2016, no. 3, pp. 1–12, 2016.

[21] B. Choe, W. Kwak, D. Jeon, and Y. Lee, "Experimental study on dynamic behavior of ball bearing cage in cryogenic environments, Part II: effects of cage mass imbalance," *Mechanical Systems and Signal Processing*, vol. 116, no. 1, pp. 25–39, 2019.

[22] S. Gao, Q. Han, N. Zhou, P. Pennacchi, and F. Chu, "Stability and skidding behavior of spacecraft porous oil-containing polyimide cages based on high-speed photography technology," *Tribology International*, vol. 165, Article ID 107294, 2022.

[23] E. Abele, L. Holland, and A. Nehrbass, "Image acquisition and image processing algorithms for movement analysis of bearing cages," *Journal of Tribology*, vol. 138, no. 2, 2016.

[24] D. Zhang, T. Wang, Q. Wang, and C. Wang, "Selectively enhanced oil retention of porous polyimide bearing materials by direct chemical modification," *Journal of Applied Polymer Science*, vol. 134, no. 29, 2017.

[25] H. I. Ruan, Y. Zhang, S. Li et al., "Effect of temperature on the friction and wear performance of porous oil-containing polyimide," *Tribology International*, vol. 157, Article ID 106891, 2021.